Polar waves and chaotic flows in thin rotating spherical shells

F. Garcia*
Department of Magnetohydrodynamics, Helmholtz-Zentrum Dresden-Rossendorf, Bautzner Landstraße 400, D-01328 Dresden, Germany and Anton Pannekoek Institute for Astronomy, University of Amsterdam, Postbus 94249, 1090 GE Amsterdam, The Netherlands

F. R. N. Chambers and A. L. Watts
Anton Pannekoek Institute for Astronomy, University of Amsterdam, Postbus 94249, 1090 GE Amsterdam, The Netherlands

(Received 27 June 2018; revised manuscript received 12 October 2018; published 8 July 2019)

Convection in rotating spherical geometries is an important physical process in planetary and stellar systems. Using continuation methods at a low Prandtl number, we find both strong equatorially asymmetric and symmetric polar nonlinear rotating waves in a model of thermal convection in thin rotating spherical shells with stress-free boundary conditions. For the symmetric waves, convection is confined to high latitude in both hemispheres but is only restricted to one hemisphere close to the pole in the case of asymmetric waves. This is in contrast to what is previously known from studies in the field. These periodic flows, in which the pattern is rotating steadily in the azimuthal direction, develop a strong axisymmetric component very close to onset. Using stability analysis of periodic orbits, the regions of stability are determined and the topology of the stable/unstable oscillatory flows bifurcated from the branches of rotating waves is described. By means of direct numerical simulations of these oscillatory chaotic flows, we show that these three-dimensional convective polar flows exhibit characteristics, such as force balance or mean physical properties, which are similar to flows occurring in planetary atmospheres. We show that these results may open a route to understanding unexplained features of gas giant atmospheres, particularly in the case of Jupiter. These include the observed equatorial asymmetry with a pronounced decrease at the equator (the so-called dimple), and the coherent vortices surrounding the poles recently observed by the Juno mission.

DOI: 10.1103/PhysRevFluids.4.074802

I. INTRODUCTION

The problem of thermal convection in rotating spherical geometries is of central importance in planetary science and astrophysics. Planetary dynamos [1], zonal jets in giant planet atmospheres [2,3], differential rotation of layers in solarlike stars [4], and convection driven by nuclear reactions in the oceans of neutron stars [5], for example, all share the key ingredients of temperature gradients, rotation, and spherical geometry. A widely used model that accounts for these factors is the Boussinesq approximation of the Navier-Stokes and energy equations in a rotating frame of reference [6]. The problem is then described by the aspect ratio $\eta = r_i/r_o$, where r_i (r_o) is the radius of the inner (outer) spherical boundary, the Prandtl, Pr, and Taylor, Ta, numbers characterize

*Corresponding author: f.garcia-gonzalez@hzdr.de

the relative importance of viscous (momentum) diffusivity to thermal diffusivity and rotational to viscous forces, respectively, and the Rayleigh number Ra is associated with buoyancy forces.

For small temperature differences between the boundaries (small Ra), heat is conducted to the outer boundary and the fluid is at rest. At a critical Rayleigh number Ra_c convection sets in, and its preferred mode pattern depends strongly on η, Pr, and Ta. In the case of the rapidly rotating ($\mathrm{Ta} > 10^{10}$) thin shells ($\eta = 0.9$), which may be appropriate for modeling Jupiter's atmosphere [7] or stellar convective oceans [8], the convective pattern strongly depends on Pr: spiraling columnar modes [9] in the bulk of the fluid for large $\mathrm{Pr} > 0.1$; equatorial inertial modes [10] lying close to the outer sphere and at low latitudes for moderate $10^{-3} < \mathrm{Pr} < 10^{-2}$; and polar modes [8,11] confined to large latitudes for both small $\mathrm{Pr} < 10^{-3}$ and moderate $10^{-2} < \mathrm{Pr} < 10^{-1}$.

Inertial modes, characteristic of small Prandtl number $\mathrm{Pr} < 1$, are explained in terms of solutions of the inviscid problem described by the Poincaré equation [10,12,13]. By increasing the size of the inner core [10], it was shown that equatorial inertial modes tend to be located at higher latitudes, especially for low wave numbers m. For a sufficiently large radius ratio, these modes can be interpreted as polar modes, as convection is restricted to high latitudes. With small but nonzero viscosity (i.e., the small Pr number thermal convection problem), the situation is similar and inertial modes located at high latitudes (polar modes) seem to be favored (instead of equatorial modes) when the radius ratio is large [8,11]. Indeed, as with inertial modes of the Poincaré equation, the onset of convection at small Pr can be antisymmetric with respect to the equator [8,11].

The large and moderate Pr number nonlinear regimes have been studied extensively [6,7,9] but low-Pr fluids of most relevance to planetary and stellar systems have received less attention. Very recently, numerical (Ref. [14] for a rotating plane layer or Refs. [15,16] for a full sphere) and laboratory [17] (cylindrical container) studies have revealed immense complexity. Low Pr convection can be strongly oscillatory even right at the onset, involving several modes, and without the appearance of the steady drifting waves that are characteristic of large Pr. Convection can even be subcritical [15] at sufficiently large Ta. The latter studies are devoted to the study of planetary cores involving nonslip boundaries, and in the case of a full rotating sphere [15] convection sets in via quasigeostrophic spiraling or equatorial modes, both being equatorially symmetric, as happens in most of the studies in rotating spherical geometry.

Low-Pr number nonlinear flows in a regime where convective onset occurs via polar equatorially antisymmetric modes have not been studied to date, and this is the main purpose of the present study. These modes are characteristic of thin shells, and have application to both stellar oceans (which may have very low $\mathrm{Pr} = 10^{-6}$ [8]) and Jupiter's atmosphere, where they may be the preferred form of onset [8]. Equatorial symmetry in three-dimensional deep convection models (which allow strong zonal jets to extend from the surface towards the planet's interior contrasting with the shallow layer approach) is a very topical issue, because the antisymmetric component of the flows is directly related to the odd gravity harmonics recently measured in Ref. [18] and used to infer the interior structure of Jupiter's atmosphere. Its strong positive jet, at around 25° latitude, dominates the antisymmetric component of the measured flow [18]. Current deep convection models of Jupiter [7] can reproduce the strong positive equatorial jet velocities and its latitudinal extend. By incorporating the effect of radiative heating of the atmosphere and magnetic dissipation deep in the atmosphere at high latitudes, Ref. [19] demonstrated that equatorial Rossby waves relate to positive equatorial jets, and that radiative effects are responsible for jets at higher latitudes. The latter studies ([7,19]) however, reproduce neither the observed Jovian equatorial asymmetry [18] (traditionally associated with the Great Red Spot [20]; see [21] for a review) nor the pronounced dimple. The latter was discussed in Ref. [22] in the context of stratified anelastic models. The anticyclonic coherent vortices observed in the giant planet's jets have been only reproduced when considering a combined shallow-water deep nonmagnetic approach [23], but again lacking equatorial asymmetry. The very recent experiments of [3] provide strong support for deep rather than shallow-water modeling. High latitude jets were obtained even when considering viscous dissipation, mimicking the expected braking of the jets due to Lorentz forces [3]. Because the polar modes studied in this paper naturally develop high latitude jets, and because the onset of convection may be of polar

type when considering nonslip boundaries [11], our results are consistent with the experiments, and provide evidence that equatorial asymmetry and high latitude jets and vortices could develop in deep convection models of spherical geometry.

We use continuation techniques [24,25] to obtain nonlinear periodic flows (rotating waves) bifurcated from the conductive motionless state, and we study their stability. This allows us to describe the patterns of the perturbations giving rise to oscillatory flows, which are obtained by means of direct numerical simulations (DNS). We adopt $\eta = 0.9$, $\mathrm{Pr} = 3 \times 10^{-3}$, and $\mathrm{Ta} = 10^7$, with stress-free boundary conditions, and we consider Ra the control parameter for our study. We emphasize that in this regime polar modes are linearly preferred [8] and the nonlinear saturation of this recently discovered instability [8,11] is still unknown. Polar modes are preferred as well for $\mathrm{Ta} > 10^{10}$, so the present study indicates the need for further research at larger Ta, which is the relevant regime for Jovian atmosphere dynamics. The paper is organized as follows. In Sec. II we introduce the formulation of the problem and the numerical method used to obtain the solutions. A brief description of the continuation method and the stability analysis of the rotating waves is provided as well (Sec. III). In Sec. IV the results are presented: the bifurcation diagrams and the patterns of the waves and their eigenfunctions are described, the study of chaotic flows is undertaken, and the application to gas giant planetary atmospheres and other physical contexts of the results is discussed (tentatively). Finally Sec. V summarizes the results.

II. MODEL

Boussinesq thermal convection in a rotating spherical shell is considered. The fluid is homogeneous with density ρ and constant physical properties: thermal diffusivity κ, thermal expansion coefficient α, and dynamic viscosity μ. The shell is defined by its inner and outer radius r_i and r_o, and it is rotating with constant angular velocity $\mathbf{\Omega} = \Omega\mathbf{k}$ about the vertical axis. A radial gravitational field $\mathbf{g} = -\gamma\mathbf{r}$ (γ is a constant and $\mathbf{r}$ is the position vector) is imposed and $\rho = \rho_0[1 - \alpha(T - T_0)]$ is assumed in just the gravitational term. In the other terms, a reference state (ρ_0, T_0) is assumed (see, for instance, [26,27]).

On the perfectly conducting boundaries, a temperature difference is imposed, $\Delta T = T_i - T_o$, $T(r_i) = T_i$, and $T(r_o) = T_o$, and stress-free boundary conditions are used for the velocity field. Stress-free conditions are appropriate for the study of planetary atmospheres [7] as well as stellar convective zones [8]. The mass, momentum, and energy equations are derived in the rotating frame of reference as in Ref. [6]. This frame of reference rotates westward, following the planetary rotation. The equations are expressed in terms of velocity ($\mathbf{v}$) and temperature ($\Theta = T - T_c$) perturbations of the basic conductive state $\mathbf{v} = \mathbf{0}$ and $T_c(r) = T_0 + \eta d\Delta T(1-\eta)^{-2}r^{-1}$, $\eta = r_i/r_o$ being the aspect ratio, $d = r_o - r_i$ being the gap width, and $T_0 = T_i - \Delta T(1-\eta)^{-1}$ being a reference temperature. With units d for the distance, $\nu^2/\gamma\alpha d^4$ for the temperature, and d^2/ν for the time, the equations are

$$\nabla \cdot \mathbf{v} = \mathbf{0}, \tag{1}$$

$$\partial_t \mathbf{v} + \mathbf{v}\cdot\nabla\mathbf{v} + 2\mathrm{Ta}^{1/2}\mathbf{k}\times\mathbf{v} = -\nabla p^* + \nabla^2\mathbf{v} + \Theta\mathbf{r}, \tag{2}$$

$$\mathrm{Pr}(\partial_t\Theta + \mathbf{v}\cdot\nabla\Theta) = \nabla^2\Theta + \mathrm{Ra}\eta(1-\eta)^{-2}r^{-3}\mathbf{r}\cdot\mathbf{v}, \tag{3}$$

where p^* is a dimensionless scalar containing all the potential forces. We neglect centrifugal effects by assuming $\Omega^2/\gamma \ll 1$, as is usual for geophysical and astrophysical applications. With the above considerations, four nondimensional parameters—the aspect ratio η and the Rayleigh Ra, Prandtl Pr, and Taylor Ta numbers—describe the physics of the problem. These numbers are defined by

$$\eta = \frac{r_i}{r_o}, \quad \mathrm{Ra} = \frac{\gamma\alpha\Delta T d^4}{\kappa\nu}, \quad \mathrm{Ta}^{1/2} = \frac{\Omega d^2}{\nu}, \quad \mathrm{Pr} = \frac{\nu}{\kappa}.$$

To solve the model equations (1)–(3) with the prescribed boundary conditions, a pseudospectral method is used (see [28] and references therein). In the radial direction, a collocation method on a Gauss-Lobatto mesh is considered, whereas spherical harmonics are used in the angular coordinates. The incompressibility condition leads to the so-called toroidal/poloidal decomposition for the velocity field [27]. The code is parallelized in the spectral and in the physical space using OpenMP directives. We use optimized libraries (FFTW3 [29]) for the fast Fourier transforms (FFTs) in longitude, and matrix-matrix products (dgemm GOTO [30]) for the Legendre transforms in latitude when computing the nonlinear terms.

High-order implicit-explicit backward differentiation formulas (IMEX-BDF) [28,31] are used for time-stepping the discretized equations. In the IMEX method, we treat the nonlinear terms explicitly in order to avoid solving nonlinear equations at each time step. The Coriolis term is treated fully implicitly to allow larger time steps. The use of *matrix-free* Krylov methods (GMRES in our case) for the linear systems facilitates the implementation of a suitable order and time step-size control. An accurate efficient time-stepper is necessary for successfully applying the continuation method due to the high resolutions required for the present study.

III. CONTINUATION METHOD AND STABILITY ANALYSIS FOR ROTATING WAVES

The study of the patterns of rotating waves (RWs) and the analysis of their stability is important because it characterizes the symmetry [32] of the oscillatory solutions (modulated rotating waves [33,34]) bifurcated from the branches (see also [35]). Indeed, the interaction of solutions of a different symmetry class (for instance, equatorial symmetry in low order models of rotating systems [36]) gives rise to complex dynamics. These secondary oscillatory solutions might play a key role in organizing the global dynamics [37] and thus chaotic flows close to the onset characteristic of low-Pr fluids [14]. The relevance of unstable RWs for the understanding of turbulent flows [38] makes their study of importance. Continuation methods are powerful as they allow the tracking of curves of unstable RWs, which cannot be obtained by means of DNS. We note that for the study of periodic, quasiperiodic, and chaotic flows (typical in thermal rotating systems [39]), mode decomposition techniques [40,41] based on DNS are a powerful tool as well, as they allow the identification of the relevant modes and patterns of the flow for very challenging problems. However, since the pioneering experiments of Hide on rotating thermal convection [42] (see [43] for a review), the scientific community has started to understand the origin of these patterns and the nature of chaotic geophysical flows using bifurcation and dynamical systems theory [32,44,45]. Continuation methods are a basic tool for their analysis [46,47], and a brief description is included in this section. The interested reader is referred to [48], or the comprehensive tutorial [25], for a theoretical description and implementation of this tool. An application of the method to thermal convection in rotating spherical shells can be found in Ref. [49]. The continuation techniques used here rely on time integrations of the Navier-Stokes plus energy equations [Eqs. (1)–(3)]. The discretized system is of dimension $n = (3L_{\max}^2 + 6L_{\max} + 1)(N_r - 1)$, $L_{\max}$ being the spherical harmonic truncation parameter and N_r the number of collocation points in the radial direction, and it takes the form

$$L_0 \partial_t u = Lu + B(u, u), \tag{4}$$

where u contains the spherical harmonic amplitudes of the toroidal, poloidal and the temperature perturbation scalars at the radial collocation mesh. Here L_0 and L are linear operators which include the boundary conditions (see [28] for details). The operator L depends on Ra (the control parameter of the present study) and includes all the linear terms and the bilinear operator B only contains the nonlinear (quadratic) terms.

To study the dependence of an azimuthally rotating wave (see [33,35] and references therein for a mathematical definition and theory of these waves), with frequency ω and with m_d-fold azimuthal symmetry, on the parameter $p = \mathrm{Ra}$, pseudo-arclength continuation methods for periodic orbits are used [48]. They allow to obtain the curve (branch) of periodic solutions $x(s) = (u(s), \tau(s), p(s)) \in \mathbb{R}^{n+2}$, u being the rotating wave, $\tau = 2\pi/(m\omega)$ the rotation period, and s the arclength parameter.

The method requires adding the pseudo-arclength condition

$$h(u, \tau, p) \equiv \langle w, x - x^0 \rangle = 0, \tag{5}$$

$x^0 = (u^0, \tau^0, p^0)$ and $w = (w_u, w_\tau, w_p)$ being the predicted point and the tangent to the curve of solutions ($\langle ., . \rangle$ stands for the inner product in $\mathbb{R}^{n+2}$), respectively, obtained by extrapolation of the previous points along the curve.

The system which determines a single solution $x = (u, \tau, p)$ on the branch is

$$H(u, \tau, p) = \begin{pmatrix} u - \phi(\tau, u, p) \\ g(u) \\ h(u, \tau, p) \end{pmatrix} = 0, \tag{6}$$

where $\phi(\tau, u, p)$ is a solution of Eqs. (1)–(3) at time $\tau = 2\pi/(m\omega)$ and initial condition u for fixed p. The condition $g(u) = 0$ is selected to fix the undetermined azimuthal phase of the rotating wave with respect to the rotating reference frame. We use $g(u) = \langle u, \partial_\varphi u_c \rangle$, where u_c is a reference solution (a previously computed rotating wave, or the preferred mode at the onset). It is a necessary condition for $\|u - u_c\|_2^2$ to be minimal with respect to the phase (see [50]). For the computation of the inner products $\langle \cdot, \cdot \rangle$ between two functions expanded in spherical harmonics, we use the definitions of [50].

To solve the large nonlinear system defined by Eq. (6), we use Newton-Krylov methods. These are matrix-free methods that do not require the explicit computation of the Jacobian $D_{(u,\tau,p)}H(u, \tau, p)$, but only its action on a given vector that consists of a time integration of a system (of dimension $2n$) obtained from the Navier-Stokes and energy equations. For the linear systems we use GMRES [51]. Due to the particular form of the spectrum of $D_{(u,\tau,p)}H(u, \tau, p)$ for dissipative systems, GMRES does not need preconditioning [48]. We note that periodic rotating waves can also be obtained efficiently by Newton-Krylov continuation methods but as steady solutions of the equations written in a reference frame that is rotating with the wave; see, for instance, Ref. [50] for thermal convection in spherical geometries or Ref. [52] for pipe flow.

The stability of a periodic solution is determined following Floquet theory [53]. It requires the computation of the dominant eigenvalues and eigenfunctions of the map $\delta u \longrightarrow D_u\phi(\tau, u, p)\delta u = v(\tau)$, with $v(\tau)$ being the solution of the first variational equation, obtained by integrating the system

$$\partial_t z = L_0^{-1}[L(p)z + B(z, z)],$$
$$\partial_t v = L_0^{-1}[L(p)v + B(z, v) + B(v, z)],$$

of dimension $2n$, with initial conditions $z(0) = u$ and $v(0) = \delta u$, over a rotation period τ, with fixed p.

The ARPACK package is used to obtain the eigenvalues of the map with a larger modulus corresponding to the dominant complex Floquet multipliers $\lambda = |\lambda| e^{i\,\mathrm{Arg}\lambda}$. Once the dominant Floquet multipliers cross the unit circle boundary ($|\lambda| > 1$), the rotating wave becomes unstable. The marginal Floquet multiplier with associated eigenfunction $v_1 = \partial_t u$ lying on the unit circle, appearing due to the invariance under azimuthal rotations, is deflated by computing the eigenvalues of the map $\delta u \longrightarrow v(\tau) - \langle v(\tau), v_1 \rangle v_1$ to avoid unnecessary computations.

We note that the method is computationally demanding because it requires the time integration of an ODE system of dimension $2n$ over one rotation period, and thus an efficient time-stepper is mandatory. Because the periodic orbit is a rotating wave there is a more efficient alternative to this procedure [50,54] that consists of studying the stability as a fixed point of a vector field.

IV. RESULTS

Planetary atmospheres and convective stellar regions have low Pr and high Ta and are modeled with thin spherical geometry $\eta = 0.9$ and stress-free boundary conditions. For a neutron star ocean, $\mathrm{Ta} > 10^{20}$ and $\mathrm{Pr} < 10^{-3}$ [8], while for the Jovian atmosphere, $\mathrm{Ta} > 10^{30}$ and $\mathrm{Pr} \lesssim 10^{-1}$ [7]. In

TABLE I. Spatial discretization study. Frequency ω, volume-averaged kinetic energy K, and dominant complex Floquet multiplier $\lambda = |\lambda| e^{i\,\mathrm{Arg}\lambda}$, vs the number of radial collocation points N_r and the spherical harmonics truncation parameter $L_{\max}$. The dimension of the system is $n = (3L_{\max}^2 + 6L_{\max} + 1)(N_r - 1)$ for the stability analysis and $n_d = [(3L_{\max}^2 + 6L_{\max})/m_d + 1](N_r - 1)$ when assuming m_d-fold azimuthal symmetry to obtain the rotating waves.

m_d	N_r	$L_{\max}$	$L_{\max}/m_d$	Ra	ω	K	$\lvert\lambda\rvert$	Argλ	n	n_d
19	30	114	6	310	169.57655	6.79415	0.996526	0.423632	1150517	60581
19	50	190	10	310	169.57656	6.79407	0.996523	0.423626	5362609	282289

addition, thermally driven liquid metal cores are not far from this regime, but the spherical shell is thick and nonslip, as is Earth's outer core [55]. According to the linear studies [8,11], equatorially antisymmetric or symmetric polar modes are good candidates to be linearly dominant in such regimes, but the nonlinear saturation of these modes has never been studied up to date. This is the purpose of the present study, which numerically investigates the finite amplitude convection at $\eta = 0.9$, $\mathrm{Pr} = 3 \times 10^{-3}$, and $\mathrm{Ta} = 10^7$. Although the latter value is still far from real applications, it belongs to the parameter regime of equatorially antisymmetric polar modes, and thus explores an exciting regime for astrophysical/planetary convection. The very large η and low Pr used lead to very challenging small spatial scales and timescales, and thus a moderate, but still relevant, Ta is considered to make the problem computationally feasible.

A. Bifurcation diagrams of polar rotating waves

According to the linear study [8], at $\eta = 0.9$, $\mathrm{Pr} = 3 \times 10^{-3}$, and $\mathrm{Ta} = 10^7$ the basic conductive state is unstable to nonaxisymmetric perturbations with $m_d = 19$ azimuthal wave number and equatorial antisymmetry located near the poles. The critical Rayleigh number is $\mathrm{Ra}_c = 3.056 \times 10^2$ and the critical frequency is $\omega_c = -3225$ (see Fig. 5 of [8]). Because the azimuthal symmetry of the basic state is broken [56], a Hopf bifurcation gives rise to a rotating wave (also called a traveling wave) drifting in the azimuthal direction with rotation frequency $\omega = -\omega_c/m_d$. We recall that any azimuthally averaged property of a rotating wave will be constant, or in other words, a rotating wave is a steady solution in the system of reference rotating with frequency ω. Notice that at the bifurcation the equatorial symmetry of the basic state is also broken, and the branch of rotating waves is then equatorially asymmetric. From now on we will use the term AP RW to denote an equatorially asymmetric polar rotating wave. In addition to the branch of AP RW that bifurcates first from the basic state, we also trace a branch of an equatorially symmetric rotating wave (SP RW from now on) associated with the second preferred $m_d = 19$ linear mode (with $\mathrm{Ra}_c = 3.25 \times 10^2$ and $\omega_c = -3169$).

The continuation method described in Sec. III is used to obtain the branch of AP RW as a function of Ra. To start the continuation process, the eigenfunction provided by the linear stability analysis [8] is used as an initial guess. We consider $N_r = 30$ radial collocation points and $L_{\max} = 114$ spherical harmonics truncation parameters with time steps around $\Delta t = 5 \times 10^{-6}$. An ($m_d = 19$)-fold azimuthal symmetry is assumed to obtain a RW to speed up the computations in the continuation process, but all of the spherical harmonics should be considered to study the stability, since the symmetry of the RW's dominant eigenfunction is unknown. The spatial resolution is increased up to $N_r = 50$, $L = 190$ to check the computations, and a comparison of several outputs of a RW at $\mathrm{Ra} = 3.1 \times 10^2$ is summarized in Table I. The values of the rotation frequency ω, volume-averaged kinetic energy $K = \frac{1}{2}\langle |\mathbf{v}|^2 \rangle_{\mathcal{V}}$, and the value of the dominant complex Floquet multiplier (from the stability analysis; see Sec. III) remain almost unchanged by increasing the resolution. As an additional numerical test, we obtain a stable AP RW by means of DNS with $N_r = 30$ and $L_{\max} = 84$, which is still well resolved, giving rise to less than a 5% difference in the kinetic energy density and rotation frequency with respect to the AP RW computed with

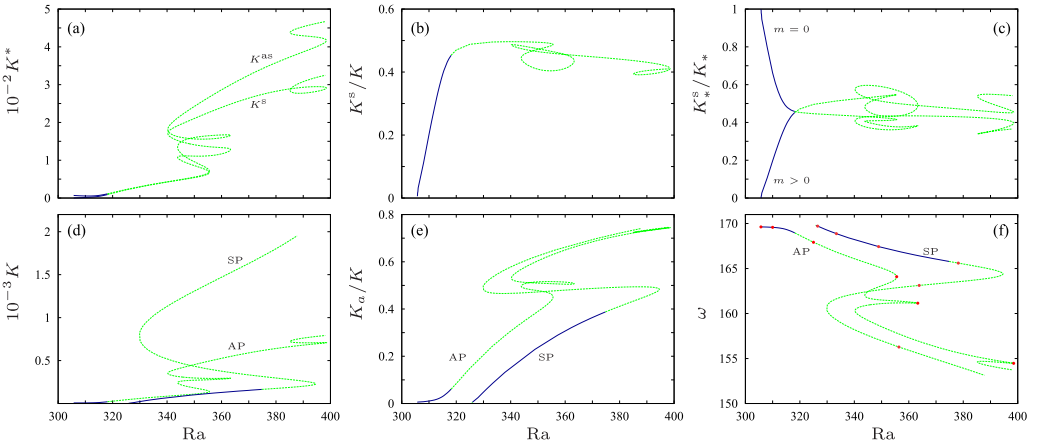

FIG. 1. Bifurcation diagrams of time- and volume-averaged quantities for varying Ra. Panels (a)–(c) are for the AP RW branch, and (d)–(f) also include the SP RW branch. (a) Kinetic energy density of the equatorially symmetric component of the flow K^{s} and of the equatorially antisymmetric part $K^{\mathrm{as}} = K - K^{\mathrm{s}}$. (b) Ratio of the equatorially symmetric kinetic energy density over total kinetic energy density K^{s}/K. (c) Ratio of the equatorially symmetric kinetic energy density of the axisymmetric ($m = 0$) flow over total axisymmetric kinetic energy density K^{s}_a/K_a and the same ratio $K^{\mathrm{s}}_{na}/K_{na}$ for the nonaxisymmetric ($m > 0$) flow. (d) Total kinetic energy density K. (e) Ratios of the axisymmetric kinetic energy over the total kinetic energy density K_a/K. (f) Rotation frequency. Solid (dashed) lines mean stable (unstable) RWs. The points (circles) of panel (f) correspond to RWs shown in Figs. 2 and 3.

continuation methods. The results for the stability analysis of the waves are validated further by filtering (i.e., time-stepping several rotation periods) the initial guess for the eigenvalue solver to avoid spurious eigenvalues (see [57] for a discussion). The number of dominant eigenvalues requested in the ARPACK package is usually 16, but we have increased the value up to 40 to check the results. With these considerations, the present study constitutes a very large application of continuation methods in fluid dynamics [58]: it investigates a large number of RWs in a regime with a large number of degrees of freedom $n = 1\,150\,517$ ($n = 5\,362\,609$, when $N_r = 50$, $L = 190$) and reveals immense complexity not explained by direct numerical simulations (DNS) but nonetheless vital for understanding real systems. Although with DNS the different mode contributions of the flow can be described, continuation techniques should be used to understand their origin. According to [37,38,44,59], turbulent flows are described in terms of unstable solutions (periodic or quasiperiodic) which cannot be captured by DNS.

Figures 1(a)–1(c) display bifurcation diagrams (of time- and volume-averaged data) for the AP branch of RWs. The stability region in each branch of the RW is marked with a solid line. The branches are started slightly above the point where they bifurcate from the conductive state [best seen in Fig. 1(a)]. This is because the convergence of the GMRES in the Newton iteration degrades when RWs are close to the onset (see [60] for an illustrative example). The kinetic energy density contained in the equatorially symmetric flow K^{S} increases from zero very sharply after the onset. The equatorially antisymmetric kinetic energy density $K^{\mathrm{AS}} = K - K^{\mathrm{S}}$ is larger in all of the branch [see Figs. 1(a) and 1(b)], meaning that the flow is strongly equatorially asymmetric very close to the onset. The axisymmetric $m = 0$ component of the flow abruptly loses its equatorially symmetry, while by contrast the nonaxisymmetric ($m > 0$) component becomes more equatorially symmetric; see Fig. 1(c). This is an unexpected result; a strong equatorially symmetric $m = 0$ flow component was found in previous studies (see, for instance, [7,22,61]) mainly at larger Pr but also at the low Pr regime [15]. Note that $K^{\mathrm{s}}_a/K_a \sim K^{\mathrm{s}}_{na}/K_{na} \in (0.3, 0.6)$. A strongly supercritical Ra regime is needed to obtain flows with $K^{\mathrm{s}}_{na}/K_{na} \in (0.3, 0.6)$ at larger Pr in thicker shells (see [61] covering

a large dynamo and hydrodynamical database), contrasting to the present study near the onset. In Figs. 1(d)–1(f), the SP RW branch is included. Its kinetic energy density is significantly larger than the corresponding value on the AP branch [see Fig. 1(d)] because convection is nearly absent in the southern hemisphere as a result of the strong equatorial asymmetry. For both AP and SP RW, the axisymmetric component of the flow [Fig. 1(e)] rises strongly, reaching almost 80% at the largest Ra explored. Strong zonal flows are characteristic of gas giants [62]. In addition, the Rossby number $\mathrm{Ro} = \mathrm{Ta}^{-1/2}\sqrt{2K} < 2 \times 10^{-2}$ is small [from Fig. 1(d)] on both branches, indicating the importance of the Coriolis force compared to inertial forces, as occurs in Jupiter's zonal flows [19]. Similar rotation frequencies (timescales) are obtained for all of the waves [Fig. 1(f)], but this is not surprising as critical frequencies at the onset are very similar.

The stability analysis, summarized in Sec. III, allows us to obtain bifurcation points on the branches. Rather than computing them accurately as in Refs. [49,50] by inverse interpolation using several points on the branches, we roughly approximate the bifurcation point to be at the point where $|\lambda| > 1$ ($|\lambda| < 1$) is satisfied for the first time. This choice makes sense, as the difference in the parameters between the previous stable (unstable) RW is small and $|\lambda| \approx 1$. The AP RW branch emerges from the preferred linear mode via supercritical Hopf bifurcation at $\mathrm{Ra}_c = 3.056 \times 10^2$, and is thus stable according to bifurcation theory [32,45]. The first bifurcation on the AP RW branch is also of Hopf type at roughly $\mathrm{Ra} = 3.18 \times 10^2$. Surprisingly, the SP RW branch has a wider stable region, from $\mathrm{Ra} = 3.26 \times 10^2$ to $\mathrm{Ra} = 3.75 \times 10^2$. The SP RW branch bifurcates unstable as it comes from the second preferred linear mode with $m_d = 19$-fold azimuthal symmetry, although this is not noticeable in Fig. 1 because SP RWs restabilize very close to the onset. This numerically proves that nonpreferred linear modes (with the same m_d-fold azimuthal symmetry as the preferred mode) contribute to stable flows, as is argued in the literature [11,63]. It is an important result as it is usual to compute only the first preferred linear mode (with fixed m_d) to determine the onset of convection [15,64–66].

A branch of stable modulated rotating waves (MRWs), which are quasiperiodic flows (see [33,34] for a theoretical description), emerges when RWs lose their stability via supercritical Hopf bifurcations at $\mathrm{Ra} = 3.18 \times 10^2$ (AP RW branch) and $\mathrm{Ra} = 3.75 \times 10^2$ (SP RW branch). In addition, stable or unstable MRWs could indeed be present near $\mathrm{Ra} = 3.26 \times 10^2$, i.e., where RWs on the SP branch become stable, depending on whether the bifurcation is subcritical or supercritical. The complex Floquet multipliers λ_k are quite clustered near the unit circle, for instance at $\mathrm{Ra} = 3.73 \times 10^2$ on the SP RW branch, $0.88 < |\lambda_k| < 1$ for the $k = 1, \ldots, 10$ first dominant multipliers. This leads to a large number of Hopf bifurcations, giving rise to oscillatory flows that can be obtained with continuation methods following [49]. Because of the large number of bifurcation points and the clustering of the eigenvalues, very long initial transients [$O(10^2)$ diffusion time units] are expected if DNS are used. Moreover, because RWs with azimuthal wave number close to $m = 19$ are also expected to be stable near the onset (see [8,49]), multistability regions of several RWs and MRWs involving different azimuthal as well as equatorial symmetries could be found, giving rise to very rich nonlinear periodic, quasiperiodic, and even chaotic dynamics very close to the onset ($\mathrm{Ra}/\mathrm{Ra}_c < 1.7$).

The azimuthal velocity v_φ patterns on the outer surface along the AP and SP branches of RW are shown in the first and second rows of Fig. 2. Convection in the southern hemisphere is progressively inhibited as Ra (i.e., nonlinearity) is increased from the onset on the AP branch. Around $\mathrm{Ra} \lesssim 3.2 \times 10^2$ RWs are stable, with most convection confined near the north pole. With increasing Ra, positive v_φ cells in the southern hemisphere increase their magnitude but remain significantly weaker than the negative v_φ cells surrounding the north pole. Along all of the AP RW branch, the kinetic energy density is concentrated near the north pole as well. This is quite an unexpected result since it is widely assumed that finite amplitude convection develops in both hemispheres (see [7,15,67,68] among many others). In the case of the SP RW, convection develops on both hemispheres as is common and, like in the AP RW branch, v_φ is positive on a wide equatorial belt and negative near the poles, the latter being stronger. Characteristic patterns of inertial waves studied in Ref. [69] can also be identified in both classes of polar waves, best shown in the meridional sections of v_φ in

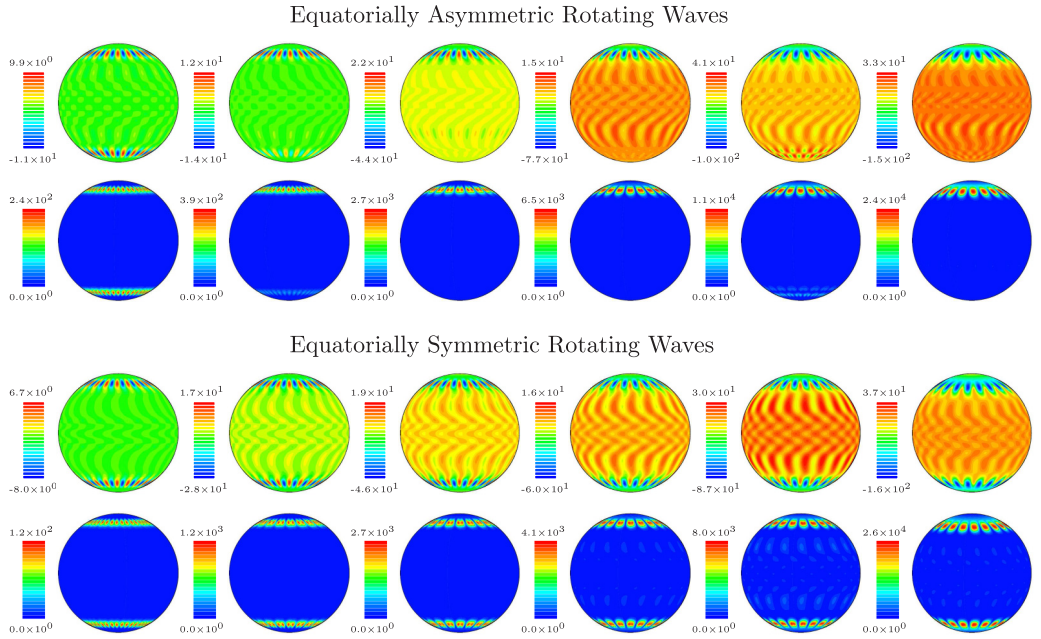

FIG. 2. First and second rows: Contour plots of $m = 19$ RW on the AP branch at $\mathrm{Ra} = 3.057 \times 10^2$, 3.1×10^2, 3.25×10^2, 3.56×10^2, 3.63×10^2, 3.99×10^2 (from left to right). First row: Spherical sections of v_ϕ at r_o. Second row: Spherical sections of $\mathbf{v}^2/2$ at r_o. Third and fourth rows: Same as the previous rows but for RW on the SP branch at $\mathrm{Ra} = 3.27 \times 10^2$, 3.33×10^2, 3.49×10^2, 3.78×10^2, 3.64×10^2, 3.56×10^2 (from left to right). All waves are marked with a circle in Fig. 1(f).

the fourth column (from left to right) of Fig. 3. These are structures elongated in the colatitudinal direction, reflecting in both boundaries and connecting the flow within the tangent cylinder from north to south latitudes. The connection of the v_φ vortices from north to south can be best identified on the spherical sections of the fourth column (from left to right) in Fig. 2.

In Fig. 4 the same contour plots as in Fig. 2 are shown for different dominant eigenfunctions at $\mathrm{Ra} = 3.2 \times 10^2$ on the AP RW branch (first row) and at $\mathrm{Ra} = 3.78 \times 10^2$ on the SP RW branch (second row). These Ra are close to the bifurcations to stable MRWs. In both branches the patterns of the first dominant eigenfunction are quite similar to that of the RW and thus similar patterns are expected for the MRW. In contrast, other eigenfunctions behave quite differently, reflecting the multimodal character of low-Pr number convection [17]. The eigenfunction patterns can be equatorially symmetric of equatorial type, or in the form of strongly axisymmetric belts surrounding the poles (see the three plots on the right). We note the good agreement of the polar belts of the eigenfunction with those obtained in the experimental study of [3] in the context of zonal flows in giant planets. In addition, this eigenfunction has convection confined within the 80° latitude circle, toward the poles, as observed on the surfaces of Jupiter [70] or Saturn [71].

B. Chaotic flows from DNS

Like the very recent low-Prandtl number studies [14,17], we find very rich quasiperiodic and even chaotic dynamics very close to the onset ($\mathrm{Ra}/\mathrm{Ra}_c < 1.7$) involving several basic modes of convection and timescales. Two examples of these strongly oscillatory DNS, obtained from an AP wave initial condition, are shown in Fig. 5 at $\mathrm{Ra} = 3.5 \times 10^2$ and $\mathrm{Ra} = 5 \times 10^2$. The left three plots of Fig. 5 are instantaneous contour plots of the temperature perturbation Θ, the azimuthal velocity v_φ, and the azimuthally averaged azimuthal velocity $\langle v_\varphi \rangle$, on a spherical slice at $r \approx r_i + 0.5d$ and

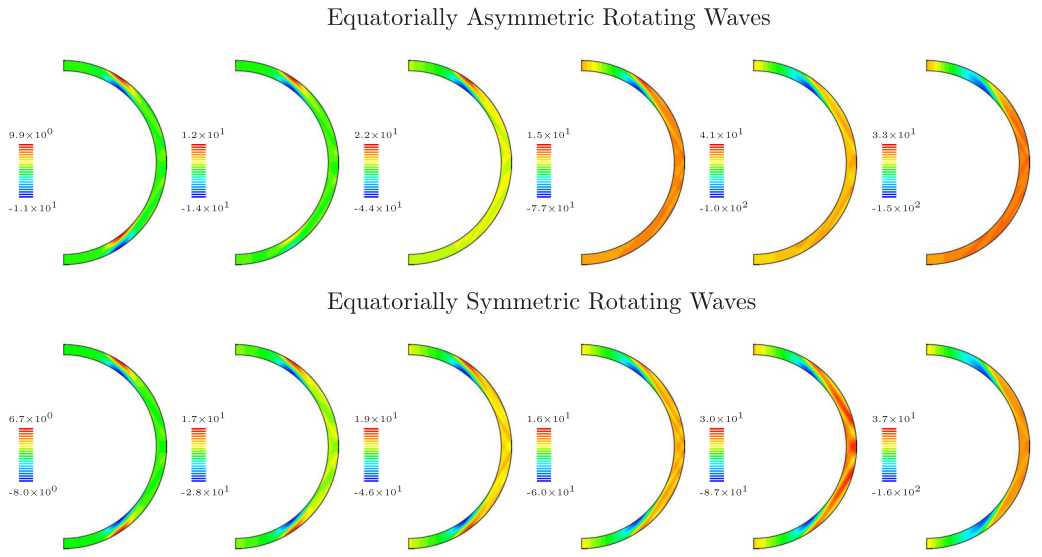

FIG. 3. Meridional sections of v_ϕ through a relative maximum. First row: Contour plots of $m = 19$ RW on the AP branch at Ra $= 3.057 \times 10^2,\ 3.1 \times 10^2,\ 3.25 \times 10^2,\ 3.56 \times 10^2,\ 3.63 \times 10^2,\ 3.99 \times 10^2$ (from left to right). Second row: Same as the previous row but for RW on the SP branch at Ra $= 3.27 \times 10^2,\ 3.33 \times 10^2,\ 3.49 \times 10^2,\ 3.78 \times 10^2,\ 3.64 \times 10^2,\ 3.56 \times 10^2$ (from left to right). All waves are marked with a circle in Fig. 1(f).

$r = r_o$, respectively, for the DNS at Ra $= 3.5 \times 10^2$. The flow is strongly equatorially asymmetric and located in polar regions, recalling an AP RW. In contrast, convection at larger Ra $= 5 \times 10^2$ (right group of three plots) also develops in the equatorial region taking the form of vertical columns. The latter resemble the patterns of the equatorial eigenfunction shown in Fig. 4. Notice that $\langle v_\varphi \rangle$ is positive in a wide band showing a strong dimple (relative minimum) near the equator.

The pattern of these DNS seems to resemble a superposition of the RW mode and the eigenfunctions shown in Fig. 2. This is not surprising, as unstable RWs and MRWs define the framework of the phase space and thus drive chaotic and turbulent dynamics [37,38,58,59]. Clearly, the flow at Ra $= 5 \times 10^2$ is strongly axisymmetric and multimodal [14,17]. Figure 6(a) displays

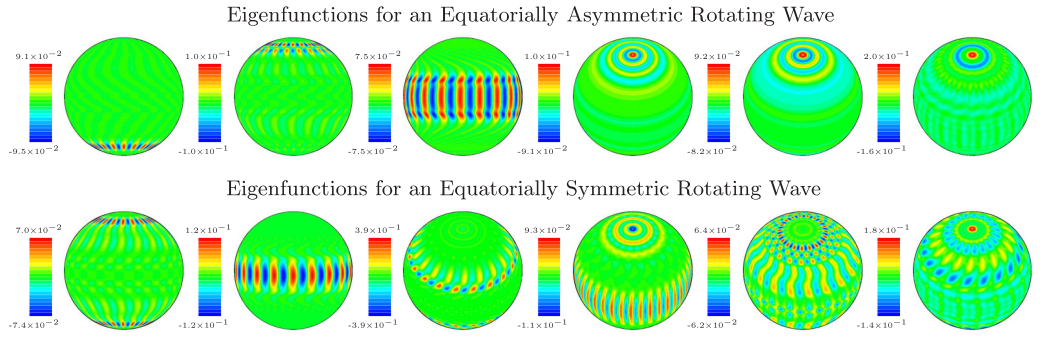

FIG. 4. First row: Contour plots of the 1st, 4th, 6th, 7th, 9th, and 13th (from left to right) dominant eigenfunctions on the AP RW branch at Ra $= 3.2 \times 10^2$. Spherical section of v_ϕ at r_o. Second row: Same as the first row but for the 1st, 2nd, 7th, 8th, 9th, and 10th dominant eigenfunctions on the SP RW branch at Ra $= 3.78 \times 10^2$.

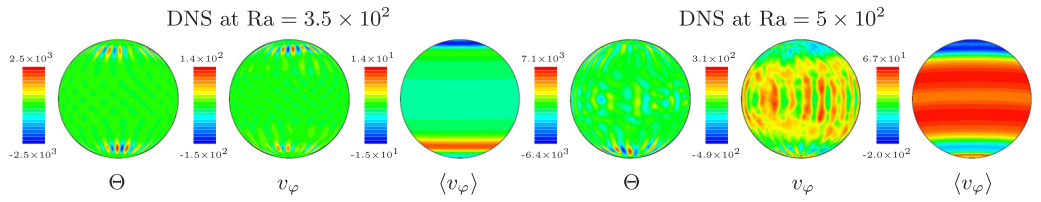

FIG. 5. Instantaneous contour plots of DNS at $\mathrm{Ra} = 3.5 \times 10^2$ (left group of three plots) and $\mathrm{Ra} = 5 \times 10^2$ (right group). For each group the spherical sections (from left to right) are of Θ (at $r \approx r_i + 0.5d$), v_φ, and $\langle v_\varphi \rangle$ (at $r = r_o$), respectively.

the time series of the convective heat transport $\mathrm{Nu} - 1$ at the outer boundary in time rotation units $t\sqrt{Ta}/2\pi$ (t is the dimensionless diffusion time). This figure, and its detail in Fig. 6(b), reveals the chaotic and strongly oscillatory character of the flow involving timescales from less than 1 to around 300 planetary rotations. Figure 6(b) contains the time span of the supplementary movie [72]. The time-averaged kinetic energy wave number spectrum is shown in Fig. 6(c), together with the corresponding theoretical Rhines' scaling [73] for the strongly axisymmetric flows relevant to planetary atmospheres. This scaling has been confirmed with a recent laboratory model, including viscous dissipation, of high latitude jets on Jupiter's surface [3]. Regarding the weakly supercritical Ra, the spectrum has a peak at the most unstable mode $m = 19$ at the onset and roughly approximates the Rhines's scaling for the larger wave numbers. The good qualitative agreement with the experimental spectrum shown in Fig. 3 of [3] is noticeable. This provides supporting evidence for the turbulent character of the DNS for the low Pr and thin shell. At higher Pr and thicker shells, corresponding to the linear stability region of equatorial or spiraling modes, higher supercritical conditions must be reached for the onset of turbulence [74,75].

C. Equatorially asymmetric zonal winds

In this section, we qualitatively analyze the equatorial symmetry of the zonal wind and describe some interesting properties of flows studied in previous sections. The study of zonal wind is of fundamental importance for the understanding of the dynamics of giant planet atmospheres [77], particularly in the case of Jupiter [7]. The Taylor number of the present study, $\mathrm{Ta} = 10^7$, is moderate and thus far from real applications. However, it is interesting to investigate basic properties of nonlinear flows arising from the onset of polar convection, as this is common in thin shells, $\eta = 0.9$ [8], which is believed to be a good geometry approximation for modeling the convective envelope of Jupiter or Saturn [77]. In thin shells, polar modes are linearly preferred also at $\mathrm{Ta} = 10^{11}$ and $\mathrm{Pr} = 10^{-2}$, very close to $\mathrm{Ta} = 10^{11}$ and $\mathrm{Pr} = 10^{-1}$ of [7], which successfully explained the number of azimuthal jets and their width in the Jovian atmosphere.

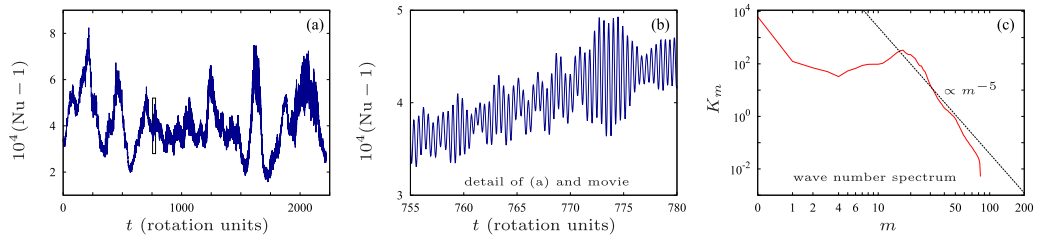

FIG. 6. (a) Time series of convective heat transfer at the outer surface $\mathrm{Nu} - 1$ and (b) a detail of (a) including the time span of the supplementary movies [72]. (c) The kinetic energy spectrum K_m vs the azimuthal wave number m and the theoretical [73] Rhines' scaling (dashed line).

TABLE II. Time- and volume-averaged properties for DNS at $\mathrm{Pr} = 3 \times 10^{-3}$, $\mathrm{Ta} = 10^7$, and $\eta = 0.9$, with Ra close to the onset of convection. The Reynolds number Re, the Rossby number Ro, the convective Rossby number Ro_c, the Peclet number Pe, and the ratio of axisymmetric ($m = 0$) over total rms kinetic energies K_a/K, and the rms of force integrals $\mathcal{F}_I$ (inertial), $\mathcal{F}_C$ (Coriolis), and $\mathcal{F}_V$ (viscous) are tabulated.

Ra	$\mathrm{Ra}/\mathrm{Ra}_c$	Re	Ro	Ro_c	Pe	K_a/K	$\mathcal{F}_C$	$\mathcal{F}_I$	$\mathcal{F}_V$
3.5×10^2	1.15	37	0.012	0.34	1.1	0.04	1.2×10^5	1.8×10^4	9.5×10^2
5×10^2	1.64	142	0.045	0.41	4.3	0.64	6.3×10^5	1.2×10^5	3.6×10^3

Flows in planetary atmospheres are turbulent and strongly axisymmetric. Some basic parameters for their study are the Reynolds number $\mathrm{Re} = \sqrt{2K}$ as a measure of convection, the Rossby number $\mathrm{Ro} = \mathrm{Ta}^{-1/2}\mathrm{Re}$ to quantify the relevance of Coriolis force [7], the convective Rossby number $\mathrm{Ro}_c = (1-\eta)^{-1/2}\sqrt{\mathrm{Ra}/(\mathrm{TaPr})}$ (the factor $1-\eta$ is due to our definition of Ra) to determine the transition between positive and negative equatorial jets [4], and the Peclet number $\mathrm{Pe} = (1-\eta)^{-1}\mathrm{Pr}\sqrt{2K}$ used to define the boundary ($\mathrm{Pe} = 10$) between weak and strong flows [15]. Flows in gas giant atmospheres have small Ro (for instance, $\mathrm{Ro} = 0.01$–0.04 given in Ref. [77]) and Ro_c less than unity ($\mathrm{Ro}_c = 0.22$ from the simulations of [77]) as their equatorial jets are positive. In addition, Pe should be large as Jupiter's and Saturn's atmospheric flows are vigorous. Table II summarizes these mean physical properties from the DNS at $\mathrm{Ra} = 3.5 \times 10^2$ and $\mathrm{Ra} = 5 \times 10^2$. Both DNS have a noticeable $\mathrm{Pe} > 1$ and thus convection is getting stronger, although they are close to the onset, as happened for similar Pr numbers in a full sphere at large Ta [15], this reflects on a relatively large Re. The Coriolis force is relevant as it indicates the small value of Ro. For $\mathrm{Ra} = 5 \times 10^2$ the ratio of axisymmetric to total kinetic energy density is relatively large, meaning the DNS is mostly axisymmetric and the equatorial zonal wind belt is positive with $\mathrm{Ro}_c = 0.41 < 1$, in reasonable agreement with [4] (at $\mathrm{Pr} = 0.27$). Following [78] the rms force, integrals $\mathcal{F}_I$ (inertial), $\mathcal{F}_C$ (Coriolis), and $\mathcal{F}_V$ (viscous) are computed. The balance $\mathcal{F}_C > \mathcal{F}_I \gg \mathcal{F}_V$, satisfied for the DNS, is believed to operate in Jupiter's convective atmosphere [19]. It is noticeable how the DNS properties detailed above are in reasonable agreement with those of giant planets, despite the fact that the parameter values are far from those objects. Larger Taylor numbers and supercritical regimes, as in Ref. [7], should be attained to study the nonlinear saturation of polar modes, which could be of interest for planetary atmospheres, as the results of Table II suggest.

Instantaneous latitude profiles of $\mathrm{Ro}_v = \langle v_\varphi \rangle / \Omega r_o$ at the outer surface for an AP and SP RW, and two examples of eigenfunctions (properly scaled), are shown in Fig. 7(a) for a qualitative comparison. Both classes of RW have off-equatorial (around 60°) negative and positive equatorial zonal bands, but the profile for the AP RW is strongly asymmetric, being positive around −60°. An eigenfunction of equatorial type gives rise to a large number of bands, with two strong relative minima and maxima for latitudes in (−20°, 20°). All of these characteristics can be identified in the equatorially asymmetric zonal wind profile of the chaotic DNS at $\mathrm{Ra} = 5 \times 10^2$; see Fig. 7(b). A suitable superposition of the profiles shown in Fig. 7(a) at lower Ra bears a reasonable resemblance to the profile of the chaotic DNS at $\mathrm{Ra} = 5 \times 10^2$, both showing a strong dimple (decrease of positive velocity) at the equator, as observed in Fig. 5. This is reasonable as branches of RWs described in this study (and secondary MRWs arising from unstable Floquet modes) may extend up to $\mathrm{Ra} = 5 \times 10^2$. The magnitude of the zonal wind clearly differs from that measured in the Jovian atmosphere. We note, however, that the decrease at the equator is larger than 50% and qualitatively comparable to the decrease observed in the Jovian atmosphere [see Fig. 7(c), revealed by Hubble Space Telescope observations [76]]. In anelastic models [22], it was argued that the dimple was related to the existence of a change in the dynamic behavior with two different flow dynamics within the shell. In our case, the situation seems to be similar, the flow being more influenced by Coriolis forces in the interior of the shell. Figure 8 (right panel) contains an equatorial section of the axial vorticity, as in Ref. [22] for the anelastic models, and displays the situation. A dashed line

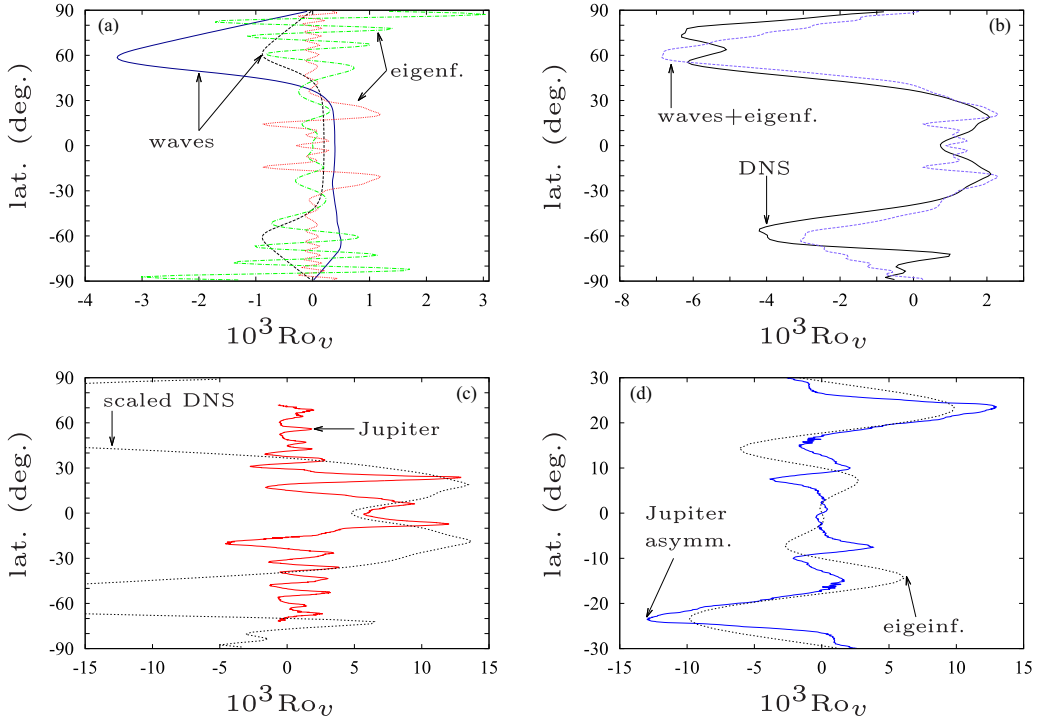

FIG. 7. $\mathrm{Ro}_v = \langle v_\varphi \rangle / \Omega r_o$ vs latitude in degrees. (a) Asymmetric polar rotating wave u_{as} at $\mathrm{Ra} = 3.98 \times 10^2$ (solid line), its eighth dominant eigenfunction (dotted-dashed line), symmetric polar rotating wave u_{s} at $\mathrm{Ra} = 3.78 \times 10^2$ (dashed line), and its $u_{2\mathrm{nd}}$ second dominant eigenfunction (dotted line). The eigenfunctions are scaled for comparative purposes. (b) DNS at $\mathrm{Ra} = 5 \times 10^2$ (solid line) and the linear superposition $u_{\mathrm{as}} + 4u_{\mathrm{s}} + 1.5 \times 10^4 u_{2\mathrm{nd}}$ of the curves of Ro_v shown in (b) (dashed line). (c) Hubble data for Jupiter [76] (solid line) and DNS of (b) scaled by a factor of 6.3 (dotted line). (d) Hubble data for the antisymmetric Jupiter zonal flow and the eighth dominant eigenfunction of the asymmetric polar rotating wave scaled by a factor of 6.5 (dotted line).

is drawn to mark the boundary between two different dynamical behaviors. Finally, Fig. 7(d) shows the Hubble Space Telescope data for the asymmetric component of the flow, compared to a selected (properly scaled) eigenfunction of an AP RW. The qualitative similarities between both profiles are noticeable, which invites further research of asymmetric modes such as those described in the present study, but at larger Ta, to see if they are relevant for understanding the equatorial asymmetry of the Jovian atmosphere [76].

Figure 8 displays instantaneous contour plots of the radial vorticity, at the outer surface in different views, of the chaotic DNS at $\mathrm{Ra} = 5 \times 10^2$. It shows the existence of large coherent vortices in the equatorial belt, but also at very high latitudes, even within the 80° circle (dashed line) toward the poles. In the Jovian atmosphere, large vortices develop in the equatorial region, as found numerically in Ref. [23] at higher $\mathrm{Ta} = 10^{11}$ with a stratified model in thin shells. Large coherent cyclonic vortices, surrounding the poles, have recently been observed in Jupiter's atmosphere [70]. Our simulated vortices at high latitudes are quite elongated in the meridional direction and obtained at moderate Ta and thus not representative of the real situation. In addition, the ratio between the number of cyclonic and anticyclonic vortices is not as large as for the Jovian atmosphere. However, our results provide evidence that cyclonic coherent vortices might be obtained at high latitudes as well as at larger Ta, since they are strongly related to AP or SP linear modes, which are preferred at relevant $\mathrm{Ta} > 10^{10}$ as well. As commented before, this makes the regime of polar modes interesting, and further challenging simulations are thus required to see if this type of convection is relevant for

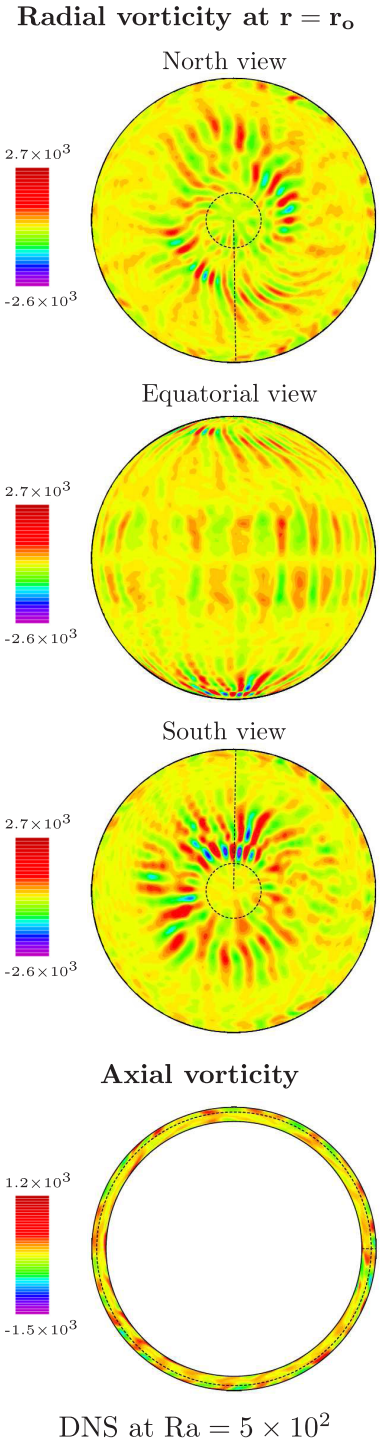

FIG. 8. Radial vorticity at $r = r_o$ (viewed from the north pole, the equator, and the south pole) and axial vorticity on the equatorial plane (from left to right). Cyclonic (anticyclonic) radial vorticity is red (blue) on the northern hemisphere and blue (red) on the southern hemisphere. A supplementary movie [72] for each panel is included.

the basic understanding of the appearance of large-scale coherent structures at high latitudes in spherical shell convection models.

V. SUMMARY

A numerical study of thermal convection in rotating spherical shells is presented. The parameter values $\eta = 0.9$, $\mathrm{Ta} = 10^7$, and $\mathrm{Pr} = 3 \times 10^{-3}$ are selected to study the unexplored regime when convection begins from equatorially antisymmetric and nonaxisymmetric polar modes [8,11]. This contrasts the regimes studied widely for many years [6,7,15,67] (among many others) in which convection starts from an equatorially symmetric and nonaxisymmetric perturbation, either equatorially attached [10,74] or spiraling [9].

As with most studies in the field [6,7,15], the numerical study is based on using DNS to obtain chaotic flows. However, there exist very few studies [50,79] in which continuation techniques and the stability analysis of periodic orbits (Floquet theory) are employed to track the curves and determine the regions of stability of rotating waves (RWs) bifurcated from the conductive state. Tracking these unstable branches is of fundamental importance for a deep understanding of the origin of chaotic and turbulent flows [37,38,44,59].

We have obtained stable equatorially asymmetric polar (AP) as well as symmetric polar (SP) RWs, the latter associated with the second dominant linear mode with $m = 19$-fold azimuthal symmetry. In this case, nonpreferred linear modes—with the same azimuthal symmetry as the preferred mode—can give rise to stable flows and should be computed in linear studies. This is relevant, as most studies have relied on the computation of the first preferred linear mode [15, 64–66] and this mode is usually used to initialize DNS with parameters close to the onset.

The patterns of the AP/SP RW are steadily rotating in the azimuthal direction, with the flow developing a strong axisymmetric component and confined at high latitudes. Surprisingly, convection is almost hemispherical in the case of AP RWs, in contrast to what has been found in previous studies. In addition, in our simulations, RWs (i.e., steadily azimuthally drifting periodic flows) are obtained at the low Pr regime and $\mathrm{Ta} = 10^7$: it is not clear if they are still present when Ta is increased; see [15] for a full sphere or the rotating convection experiments of [17].

By means of DNS at $\mathrm{Ra}/\mathrm{Ra}_c < 1.7$, oscillatory chaotic flows are obtained, in agreement with low-Prandtl number studies [14,15,17]. Their dynamics are strongly influenced by unstable RWs and quasiperiodic flows (modulated rotating waves), related to the eigenfunctions of the RWs, as our numerical results suggest. Computation of stable/unstable waves then provides a useful tool to understand the dynamics of turbulent flows [38,44].

In addition, these oscillatory flows reveal physical regimes that share qualitative characteristics with those occurring in the Jovian atmosphere. They have strong zonal and equatorially asymmetric components, including the presence of polar coherent vortices [70] and the characteristic dimple [76]. Although the value $\mathrm{Ta} = 10^7$ of our models is still small, the force balance of the simulations is in concordance with that believed to operate in the planetary atmospheres, and the flow physical properties such as the Rossby number [7] or the convective Rossby number [4] are not so far from their estimated values. Our study indicates the need for further research at more relevant $\mathrm{Ta} > 10^{10}$, as polar convection is linearly preferred also in this regime.

Our results may also be relevant in explaining the coherent structures without equatorial symmetry, vortices, observed on Saturn's polar surface in late 2012 by the Cassini spacecraft [71]. The polar convection is known to grow in strongly nonlinear regimes [62], but we have shown the existence of polar flows at very low Rayleigh numbers. Our results may also help with the understanding of planetary core dynamos, as AP modes may be preferred at the onset with nonslip conditions [11]. According to [61], equatorially asymmetric flows favor the appearance of multipolar magnetic fields, which have been shown to be characteristic of thin shells [80,81]. Understanding the equatorial symmetry breaking of the flow and its associated transitions is then of importance in planetary dynamo numerical models.

Because very low Pr and large η are common in stellar convective zones [8], our results are also of importance for the astrophysical community. A transition between positive and negative zonal flow profiles was found in Ref. [4] in the context of stellar magnetohydrodynamic flows, such as those appearing in the Sun. In the case of accreting neutron star oceans, convection [82], zonal flows [83], pattern formation, and coherent structures [5] are key issues for a deeper understanding of thermonuclear x-ray bursting phenomena.

ACKNOWLEDGMENTS

F.G. was supported by a postdoctoral fellowship of the Alexander von Humboldt Foundation. The authors acknowledge support from ERC Starting Grant No. 639217 CSINEUTRONSTAR (P.I.W.). This work was sponsored by NWO Exact and Natural Sciences for the use of supercomputer facilities with the support of SURF Cooperative, Cartesius pilot project 16320-2018. The authors wish to thank F. Stefani, M. Net, and J. Sánchez for useful discussions.

[1] *Mathematical Aspects of Natural Dynamos*, edited by E. Dormy and A. M. Soward, The Fluid Mechanics of Astrophysics and Geophysics Vol. 13 (Chapman & Hall/CRC, Boca Raton, FL, 2007).
[2] C. A. Jones and K. M. Kuzanyan, Compressible convection in the deep atmospheres of giant planets, Icarus **204**, 227 (2009).
[3] S. Cabanes, J. Aurnou, B. Favier, and M. Le Bars, A laboratory model for deep-seated jets on the gas giants, Nat. Phys. **13**, 387 (2017).
[4] J. Mabuchi, Y. Masada, and A. Kageyama, Differential rotation in magnetized and non-magnetized stars, Astrophys. J. **806**, 1 (2015).
[5] A. L. Watts, Thermonuclear burst oscillations, Ann. Rev. Astron. Astrophys. **50**, 609 (2012).
[6] R. Simitev and F. H. Busse, Patterns of convection in rotating spherical shells, New J. Phys **5**, 97 (2003).
[7] M. Heimpel, J. Aurnou, and J. Wicht, Simulation of equatorial and high-latitude jets on Jupiter in a deep convection model, Nature (London) **438**, 193 (2005).
[8] F. Garcia, F. R. N. Chambers, and A. L. Watts, The onset of low Prandtl number thermal convection in thin spherical shells, Phys. Rev. Fluids **3**, 024801 (2018).
[9] K. Zhang, Spiralling columnar convection in rapidly rotating spherical fluid shells, J. Fluid Mech. **236**, 535 (1992).
[10] K. Zhang, On equatorially trapped boundary inertial waves, J. Fluid Mech. **248**, 203 (1993).
[11] F. Garcia, J. Sánchez, and M. Net, Antisymmetric Polar Modes of Thermal Convection in Rotating Spherical Fluid Shells at High Taylor Numbers, Phys. Rev. Lett. **101**, 194501 (2008).
[12] K. Zhang, On coupling between the Poincaré equation and the heat equation, J. Fluid Mech. **268**, 211 (1994).
[13] F. H. Busse and R. Simitev, Inertial convection in rotating fluid spheres, J. Fluid Mech. **498**, 23 (2004).
[14] S. Horn and P. J. Schmid, Prograde, retrograde, and oscillatory modes in rotating Rayleigh-Bénard convection, J. Fluid Mech. **831**, 182 (2017).
[15] E. J. Kaplan, N. Schaeffer, J. Vidal, and P. Cardin, Subcritical Thermal Convection of Liquid Metals in a Rapidly Rotating Sphere, Phys. Rev. Lett. **119**, 094501 (2017).
[16] K. Lam, D. Kong, and K. Zhang, Nonlinear thermal inertial waves in rotating fluid spheres, Geophys. Astrophys. Fluid Dyn. **112**, 357 (2018).
[17] J. M. Aurnou, V. Bertin, A. M. Grannan, S. Horn, and T. Vogt, Rotating thermal convection in liquid gallium: multi-modal flow, absent steady columns, J. Fluid Mech. **846**, 846 (2018).
[18] Y. Kaspi *et al.*, Jupiter's atmospheric jet streams extend thousands of kilometres deep, Nature (London) **555**, 223 (2018).
[19] T. Schneider and J. Liu, Formation of jets and equatorial superrotation on Jupiter, J. Atmos. Sci. **66**, 579 (2009).

[20] P. L. Read and R. Hide, Long-lived eddies in the laboratory and in the atmospheres of Jupiter and Saturn, Nature (London) **302**, 126 (1983).
[21] P. S. Marcus, Jupiter's Great Red Spot and other vortices, Ann. Rev. Astron. Astrophys. **31**, 523 (1993).
[22] T. Gastine, J. Wicht, and J. M. Aurnou, Zonal flow regimes in rotating anelastic spherical shells: An application to giant planets, Icarus **225**, 156 (2013).
[23] M. Heimpel, T. Gastine, and J. Wicht, Simulation of deep-seated zonal jets and shallow vortices in gas giant atmospheres, Nat. Geosci. **9**, 19 (2015).
[24] H. B. Keller, Numerical solution of bifurcation and nonlinear eigenvalue problems, in *Applications of Bifurcation Theory*, edited by P. H. Rabinowitz (Academic, New York, 1977), pp. 359–384.
[25] J. Sánchez and M. Net, Numerical continuation methods for large-scale dissipative dynamical systems, Eur. Phys. J. Spec. Top. **225**, 2465 (2016).
[26] J. Pedlosky, *Geophysical Fluid Dynamics* (Springer Verlag, New York, 1979).
[27] S. Chandrasekhar, *Hydrodynamic and Hydromagnetic Stability* (Dover, New York, 1981).
[28] F. Garcia, M. Net, B. García-Archilla, and J. Sánchez, A comparison of high-order time integrators for thermal convection in rotating spherical shells, J. Comput. Phys. **229**, 7997 (2010).
[29] M. Frigo and S. G. Johnson, The design and implementation of FFTW3, Proc. IEEE **93**, 216 (2005), special issue on "Program Generation, Optimization, and Platform Adaptation" .
[30] K. Goto and R. A. van de Geijn, Anatomy of high-performance matrix multiplication, ACM Trans. Math. Softw. **34**, 1 (2008).
[31] F. Garcia, M. Net, and J. Sánchez, A comparison of high-order time integrators for highly supercritical thermal convection in rotating spherical shells, in *Proceedings of the International Conference on Spectral and High Order Methods for Partial Differential Equations-ICOSAHOM 2013, Lecture Notes in Computational Science and Engineering*, edited by J. S. Hesthaven, M. Azaïez, and H. El Fekih (Springer, New York, 2014), Vol. 95.
[32] J. D. Crawford and E. Knobloch, Symmetry and symmetry-breaking bifurcations in fluid dynamics, Annu. Rev. Fluid Mech. **23**, 341 (1991).
[33] D. Rand, Dynamics and symmetry. Predictions for modulated waves in rotating fluids, Arch. Ration. Mech. An. **79**, 1 (1982).
[34] K. T. Coughlin and P. S. Marcus, Modulated waves in Taylor-Couette flow. Part 1. Analysis, J. Fluid Mech. **234**, 1 (1992).
[35] M. Golubitsky, V. G. LeBlanc, and I. Melbourne, Hopf bifurcation from rotating waves and patterns in physical space, J. Nonlin. Sci. **10**, 69 (2000).
[36] E. Knobloch and A. S. Landsberg, A new model of the solar cycle, Mon. Not. R. Astron. Soc. **278**, 294 (1996).
[37] G. Kawahara, M. Uhlmann, and L. van Veen, The significance of simple invariant solutions in turbulent flows, Arch. Ration. Mech. An. **44**, 203 (2012).
[38] B. Hof *et al.*, Experimental observation of nonlinear traveling waves in turbulent pipe flow, Science **305**, 1594 (2004).
[39] R. Hide, S. R. Lewis, and P. L. Read, Sloping convection: A paradigm for large-scale waves and eddies in planetary atmospheres, CHAOS **4**, 135 (1994).
[40] M. Williams, P. Schmid, and J. Kutz, Hybrid reduced-order integration with proper orthogonal decomposition and dynamic mode decomposition, Multiscale Model. Simul. **11**, 522 (2013).
[41] S. Le Clainche and J. Vega, Higher order dynamic mode decomposition, SIAM J. Appl. Dynam. Syst. **16**, 882 (2017).
[42] R. Hide, Some experiments on thermal convection in a rotating liquid, Quart. J. R. Meteor. Soc. **79**, 161 (1953).
[43] M. Ghil, P. Read, and L. Smith, Geophysical flows as dynamical systems: the influence of hide's experiments, Astron. Geophys. **51**, 428 (2010).
[44] D. Ruelle and F. Takens, On the nature of turbulence, Commun. Math. Phys. **20**, 167 (1971).
[45] Y. A. Kuznetsov, *Elements of Applied Bifurcation Theory*, 2nd ed. (Springer, New York, 1998).
[46] E. Doedel, *AUTO: Software for continuation and bifurcation problems in ordinary differential equations*, Report Applied Mathematics, California Institute of Technology, Pasadena, CA (1986).

[47] *Numerical Methods for Bifurcation Problems and Large-Scale Dynamical Systems*, IMA Volumes in Mathematics and its Applications Vol. 119, edited by E. Doedel and L. S. Tuckerman (Springer-Verlag, Berlin, 2000).
[48] J. Sánchez, M. Net, B. García-Archilla, and C. Simó, Newton-Krylov continuation of periodic orbits for Navier-Stokes flows, J. Comput. Phys. **201**, 13 (2004).
[49] F. Garcia, M. Net, and J. Sánchez, Continuation and stability of convective modulated rotating waves in spherical shells, Phys. Rev. E **93**, 013119 (2016).
[50] J. Sánchez, F. Garcia, and M. Net, Computation of azimuthal waves and their stability in thermal convection in rotating spherical shells with application to the study of a double-Hopf bifurcation, Phys. Rev. E **87**, 033014 (2013).
[51] Y. Saad and M. H. Schultz, GMRES: A generalized minimal residual algorithm for solving nonsymmetric linear systems, SIAM J. Sci. Stat. Comput. **7**, 856 (1986).
[52] L. S. Tuckerman, J. Langham, and A. Willis, Order-of-magnitude speedup for steady states and traveling waves via stokes preconditioning in channel flow and open pipe flow, in *Computational Modelling of Bifurcations and Instabilities in Fluid Dynamics* (Springer International, Cham, Switzerland, 2019), pp. 3–31.
[53] D. Jordan and P. Smith, *Nonlinear Ordinary Differential Equations: An Introduction for Scientists and Engineers*, Oxford Texts in Applied and Engineering Mathematics (Oxford University Press, Oxford, 2007), Vol. 10.
[54] L. S. Tuckerman, Laplacian preconditioning for the inverse Arnoldi method, Commun. Comput. Phys. **18**, 1336 (2015).
[55] C. A. Jones, Planetary magnetic fields and fluid dynamos, Annu. Rev. Astron. Astrophys. **43**, 583 (2011).
[56] R. E. Ecke, F. Zhong, and E. Knobloch, Hopf bifurcation with broken reflection symmetry in rotating Rayleigh-Bénard convection, Europhys. Lett. **19**, 177 (1992).
[57] J. Sánchez, F. Garcia, and M. Net, Radial collocation methods for the onset of convection in rotating spheres, J. Comput. Phys. **308**, 273 (2016).
[58] H. A. Dijkstra, F. W. Wubs, A. K. Cliffe, E. Doedel, I. F. Dragomirescu, B. Eckhardt, A. Y. Gelfat, A. L. Hazel, V. Lucarini, A. G. Salinger, E. T. Phipps, J. Sánchez-Umbría, H. Schuttelaars, L. S. Tuckerman, and U. Thiele, Numerical bifurcation methods and their application to fluid dynamics: Analysis beyond simulation, Commun. Comput. Phys. **15**, 1 (2014).
[59] J.-P. Eckmann, Roads to turbulence in dissipative dynamical systems, Rev. Mod. Phys. **53**, 643 (1981).
[60] J. Sánchez and M. Net, Continuation of bifurcations of periodic orbits for large-scale systems, SIAM J. Appl. Dyn. Syst. **14**, 678 (2015).
[61] F. Garcia, L. Oruba, and E. Dormy, Equatorial symmetry breaking and the loss of dipolarity in rapidly rotating dynamos, Geophys. Astrophys. Fluid Dyn. **111**, 380 (2017).
[62] U.R. Christensen, Zonal flow driven by strongly supercritical convection in rotating spherical shells, J. Fluid Mech. **470**, 115 (2002).
[63] M. Landeau and J. Aubert, Equatorially asymmetric convection inducing a hemispherical magnetic field in rotating spheres and implications for the past martian dynamo, Phys. Earth Planet. Inter. **185**, 61 (2011).
[64] F. M. Al-Shamali, M. H. Heimpel, and J. M. Aurnou, Varying the spherical shell geometry in rotating thermal convection, Geophys. Astrophys. Fluid Dyn. **98**, 153 (2004).
[65] E. Dormy, A. M. Soward, C. A. Jones, D. Jault, and P. Cardin, The onset of thermal convection in rotating spherical shells, J. Fluid Mech. **501**, 43 (2004).
[66] J. Vidal and N. Schaeffer, Quasi-geostrophic modes in the Earth's fluid core with an outer stably stratified layer, Geophys. J. Int. **202**, 2182 (2015).
[67] F. H. Busse, Thermal instabilities in rapidly rotating systems, J. Fluid Mech. **44**, 441 (1970).
[68] M. Ardes, F. H. Busse, and J. Wicht, Thermal convection in rotating spherical shells, Phys. Earth Planet. Inter. **99**, 55 (1997).
[69] M. Rieutord and L. Valdettaro, Inertial waves in a rotating spherical shell, J. Fluid Mech. **341**, 7799 (1997).
[70] A. Adriani *et al.*, Clusters of cyclones encircling Jupiter's poles, Nature (London) **555**, 216 (2018).

[71] K. M. Sayanagi, J. J. Blalock, U. A. Dyudina, S. P. Ewald, and A. P. Ingersoll, Cassini ISS observation of Saturn's north polar vortex and comparison to the south polar vortex, Icarus **285**, 68 (2017).
[72] See Supplemental Material at http://link.aps.org/supplemental/10.1103/PhysRevFluids.4.074802 for movies displaying the time evolution of contour plots shown in each panel of Fig. 8.
[73] P. B. Rhines, Waves and turbulence on a beta-plane, J. Fluid Mech. **69**, 417 (1975).
[74] E. Plaut and F. H. Busse, Multicellular convection in rotating annuli, J. Fluid Mech. **528**, 119 (2005).
[75] F. Garcia, J. Sánchez, and M. Net, Numerical simulations of thermal convection in rotating spherical shells under laboratory conditions, Phys. Earth Planet. Inter. **230**, 28 (2014).
[76] J. Tollefson, M. H. Wong, I. d. Pater, A. A. Simon, G. S. Orton, J. H. Rogers, S. K. Atreya, R. G. Cosentino, W. Januszewski, R. Morales-Juberías, and P. S. Marcus, Changes in Jupiter's zonal wind profile preceding and during the Juno mission, Icarus **296**, 163 (2017).
[77] M. Heimpel and J. Aurnou, Turbulent convection in rapidly rotating spherical shells: A model for equatorial and high latitude jets on Jupiter and Saturn, Icarus **187**, 540 (2007).
[78] K. M. Soderlund, E. M. King, and J. M. Aurnou, The influence of magnetic fields in planetary dynamo models, Earth Planet. Sci. Lett. **333-334**, 9 (2012).
[79] F. Feudel, L. S. Tuckerman, M. Gellert, and N. Seehafer, Bifurcations of rotating waves in rotating spherical shell convection, Phys. Rev. E **92**, 053015 (2015).
[80] M. Schrinner, L Petitdemange, and E. Dormy, Dipole collapse and dynamo waves in global direct numerical simulations, Astrophys. J. **752**, 1 (2012).
[81] L. Oruba and E. Dormy, Transition between viscous dipolar and inertial multipolar dynamos, Geophys. Res. Lett. **41**, 7115 (2014).
[82] M. Zingale, C. M. Malone, A. Nonaka, A. S. Almgren, and J. B. Bell, Comparisons of two- and three-dimensional convection in type I x-ray bursts, Astrophys. J. **807**, 60 (2015).
[83] A. Spitkovsky, Y. Levin, and G. Ushomirsky, Propagation of thermonuclear flames on rapidly rotating neutron stars: Extreme weather during type I x-ray bursts, Astrophys. J. **566**, 1018 (2002).